Comparison of Multiresolution Features for Texture Classification of Carotid Atherosclerosis From B-Mode Ultrasound

Nikolaos N. Tsiaparas, Spyretta Golemati, *Member, IEEE*, Ioannis Andreadis, John S. Stoitsis, *Member, IEEE*, Ioannis Valavanis, *Member, IEEE*, and Konstantina S. Nikita, *Senior Member, IEEE*

***Abstract*—In this paper, a multiresolution approach is suggested for texture classification of atherosclerotic tissue from B-mode ultrasound. Four decomposition schemes, namely, the discrete wavelet transform, the stationary wavelet transform, wavelet packets (WP), and Gabor transform (GT), as well as several basis functions, were investigated in terms of their ability to discriminate between symptomatic and asymptomatic cases. The mean and standard deviation of the detail subimages produced for each decomposition scheme were used as texture features. Feature selection included 1) ranking the features in terms of their divergence values and 2) appropriately thresholding by a nonlinear correlation coefficient. The selected features were subsequently input into two classifiers using support vector machines (SVM) and probabilistic neural networks. WP analysis and the coiflet 1 produced the highest overall classification performance (90% for diastole and 75% for systole) using SVM. This might reflect WP's ability to reveal differences in different frequency bands, and therefore, characterize efficiently the atheromatous tissue. An interesting finding was that the dominant texture features exhibited horizontal directionality, suggesting that texture analysis may be affected by biomechanical factors (plaque strains).**

***Index Terms*—Carotid, texture, ultrasound, wavelet transforms.**

I. Introduction

THE instability of the carotid atheromatous plaque has been shown to be associated not only with the degree of stenosis but also with plaque echogenicity estimated from B-mode ultrasound images [1]. Plaque echogenicity through image texture analysis has been analyzed with a number of mostly statistical methods ([2] and [3]), among which the gray scale median (GSM) has been extensively used in the study of various aspects of vascular disease ([4] and [5]). The fractal dimension, a model-based technique, was also used in two studies ([3] and [6]) to differentiate between symptomatic and asymptomatic cases. For a comprehensive review on texture analysis and classification of carotid atheromatous plaque from B-mode ultrasound see also [7].

Manuscript received April 30, 2010; revised September 22, 2010; accepted October 29, 2010. Date of publication November 11, 2010; date of current version January 4, 2011.

N. N. Tsiaparas, I. Andreadis, J. S. Stoitsis, I. Valavanis, and K. S. Nikita are with the Department of Electrical and Computer Engineering, National Technical University of Athens, Athens 15780, Greece (e-mail: ntsiapar@biosim.ntua.gr).

S. Golemati is with the Medical School, National Kapodistrian University of Athens, Athens 10675, Greece (e-mail: sgolemati@med.uoa.gr).

Digital Object Identifier 10.1109/TITB.2010.2091511

The spatial distribution of gray levels in a plaque ultrasound image, estimated using texture, is determined by the distribution of echogenic (fibrous and calcified tissue) and anechoic (blood and lipids) materials within the plaque. Such distributions may be characterized by 1) low frequencies, i.e., slow changes in gray levels; these may correspond to large areas occupied by a specific type material; or 2) high frequencies, i.e., rapid changes in gray levels; these may correspond to different materials randomly scattered within the plaque. In reality, however, texture measures describe not only the underlying material distribution but also the effect of speckle that is due to the coherent formation of the echo from many scatterers randomly distributed within the resolution cell. Although speckle is considered as noise, it is not typical random noise and may carry useful image information [8]. It is believed that speckle is a high-frequency component of the image. Consequently, the use of a scale/frequency approach, based, for example, on wavelet transforms, which decompose appropriately the frequency content of the image, may reveal plaque texture characteristics free from the effect of speckle noise.

Wavelet models have been used in a number of texture classification tasks not only in reference (e.g., Brodatz) but also in real medical images. The discrete wavelet transform (DWT) has been used to characterize myocardial [9] and breast [10] tissue from ultrasound images. The stationary wavelet transform (SWT), a modified time-invariant version of DWT, has been suggested for texture classification tasks [11]. Wavelet packets (WP), a modification of the DWT consisting of more detailed decomposition steps, are also commonly encountered in wavelet-based texture classification studies [12]. In ultrasound imaging tasks, WP decomposition has been applied to discriminate between benign and malignant liver tumors [13]. Finally, Gabor transform (GT), a family of linear, frequency-, and orientation-selective filters particularly appropriate for texture representation and discrimination, have been used to characterize carotid atheromatous plaque tissue from B-mode ultrasound [14].

The purpose of this paper was to investigate the possibility of the wavelet transform to characterize and classify the texture of ultrasound images of carotid atheromatous plaque. To this end, four different wavelet decomposition schemes, the DWT, SWT, WP, and GT as well as a number of basis functions derived from different wavelet families, were benchmarked, in terms of their ability to discriminate between symptomatic and asymptomatic cases. Probabilistic neural networks (PNN) and support vector machines (SVM), both recently used for the classification of

morphological features of carotid atherosclerotic plaque [15], were used as classifiers.

II. Image Multiresolution Analysis

Images usually contain information at multiple resolutions. Multiresolution image analysis, including wavelet-based methods, has emerged as a useful framework for many image analysis tasks and consists in representing image details of different sizes at appropriate resolution scales.

A. Discrete Wavelet Transform

The DWT of a signal $x[n]$ is defined as its inner product with a family of functions, $\varphi_{j,k}(t)$ and $\psi_{j,k}(t)$, which form an orthonormal set of vectors, a combination of which can completely define the signal, and hence, allow its analysis in many resolution levels j [16]

$$\varphi_{j,k}(t) = 2^{j/2}\varphi(2^j t - k) \quad \psi_{j,k}(t) = 2^{j/2}\psi\left(2^j t - k\right). \quad (1)$$

The functions $\varphi_{j,k}(t)$ and $\psi_{j,k}(t)$ consist of versions of the prototype scaling $\varphi(t)$ and wavelet $\psi(t)$ functions, discretized at level j and at translation k. However, for the implementation of the DWT, only the coefficients of two half-band filters: a low-pass $h(k)$ and a high-pass $g(k) = (-1)^k h(1-k)$ filter, are required, which satisfy the following conditions:

$$\varphi_{j+1,0}(t) = \sum_k h[k] \cdot \varphi_{j,k} \quad \psi_{j+1,0}(t) = \sum_k g[k] \cdot \psi_{j,k}. \quad (2)$$

Hence, the DWT is defined as follows:

$$A_{j+1,n} = \sum_k A_{j,k} \cdot h_j[k-2n]$$
$$D_{j+1,n} = \sum_k A_{j,k} \cdot g_j[k-2n] \quad (3)$$

where $A_{j,n}$ and $D_{j,n}$ are known as the approximation and detail coefficients, respectively, at level j and location n. According to (3), the outputs $A_{j,n}$ and $D_{j,n}$ of the convolution are downsampled by two for every level of analysis, where the time resolution is halved and the frequency resolution is doubled.

For images, i.e., 2-D signals, the 2-D DWT can be used. This consists of a DWT on the rows of the image and a DWT on the columns of the resulting image. The result of each DWT is followed by downsampling on the columns and rows, respectively. The decomposition of the image yields four subimages for every level.

Fig. 1(a) shows a schematic diagram of the 2-D DWT for a given level of analysis. Each approximation subimage (A_j) is decomposed into four subimages [A_{j+1}, Dh_{j+1}, Dv_{j+1}, and Dd_{j+1} in Fig. 1(a)], according to the previously described scheme. Each detail subimage is the result of a convolution with two half-band filters: a low-pass and a high-pass for Dh_j, a high-pass and a low-pass for Dv_j, and two high-pass filters for Dd_j.

B. Stationary Wavelet Transform

The 2-D SWT is similar to the 2-D DWT, but no downsampling is performed. Instead, upsampling of the low-pass and high-pass filters is carried out [see Fig. 1(b)]. The main advantage of SWT over DWT is its shift invariance property. However, it is nonorthogonal and highly redundant, and hence, computationally expensive.

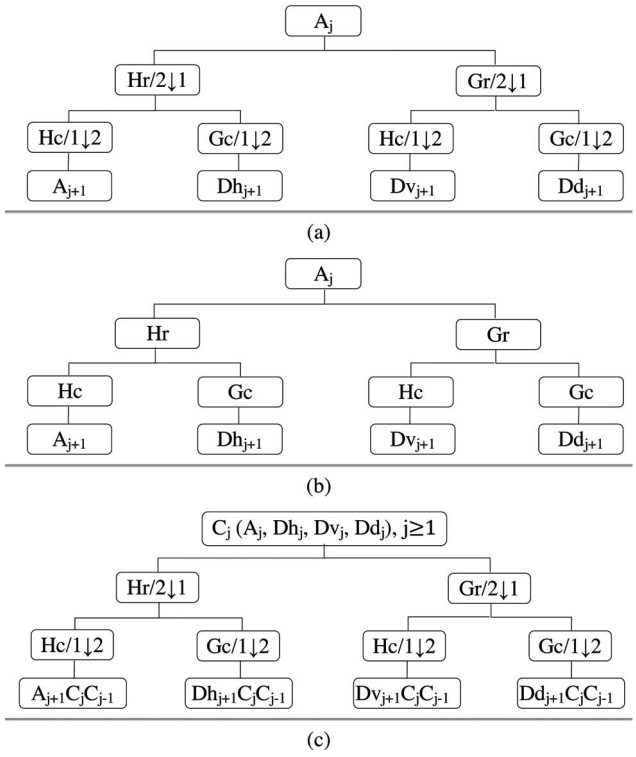

Fig. 1. Schematic diagram of the (a) 2-D DWT, (b) SWT, and (c) WP decomposition schemes for a given level of analysis. Note that, for $j = 0$, A_0 is the original image, whereas for $j = 1$, C_0 is omitted from the abbreviation of WP subimages. Hr, Hc, Gr, and Gc are the low-pass and high-pass filters on the rows and columns of each subimage. The symbols "2↓1" and "1↓2" denote the downsampling procedure on the columns and rows, respectively, which is valid for DWT and WP only.

C. Wavelet Packet Decomposition

The 2-D WP decomposition is a simple modification of the 2-D DWT, which offers a richer space-frequency representation. The first level of analysis is the same as that of the 2-D DWT. The second, as well as all subsequent levels of analysis consist of decomposing every subimage, rather than only the approximation subimage, into four new subimages [see Fig. 1(c)].

D. Gabor Transform

The GT of an image consists in convolving that image with the Gabor function, i.e., a sinusoidal plane wave of a certain frequency and orientation modulated by a Gaussian envelope. Frequency and orientation representations of Gabor filters are similar to those of the human visual system, rendering them appropriate for texture segmentation and classification.

III. Material and Methods

A. Subjects and Ultrasound Image Data

A total of 20 atheromatous plaques were investigated, of which 11 were symptomatic and 9 asymptomatic. Symptoms

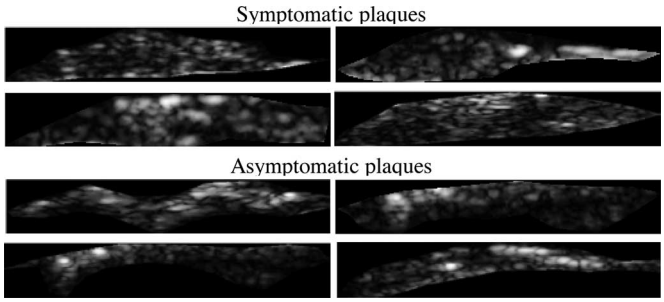

Fig. 2. Examples of plaque ROIs manually segmented from B-mode ultrasound images for symptomatic and asymptomatic plaques. Examples correspond to a systolic (left) and diastolic (right) phase of the cardiac cycle.

included stroke, hemispheric transient ischemic attack, and amaurosis fugax. There was no significant difference in the degrees of stenosis between the two groups of plaques (67.7% $\pm$ 15.1% in symptomatic and 67.2% $\pm$ 13.2% in asymptomatic plaques, Wilcoxon test, p-value $= 0.93$).

For each subject, a sequence of longitudinal images was recorded with an Advanced Technology Laboratory (ATL) Ultramark 4 Duplex scanner and a high resolution 7.5 MHz linear scan head. Scanner settings (dynamic range 60 dB, 2-D gray map, persistence low, and frame rate high) were set at the beginning of the recording and not altered during the procedure. The sequences were recorded at a rate of 25 frames/s for approximately 3 s (2–3 cardiac cycles) during breath holding.

From each sequence, two static images were isolated corresponding to specific instants of the cardiac cycle, namely, systole and diastole. Static images at selected instants of the cardiac cycle were isolated from the recorded image sequences using the motion analysis methodology described in [17]. Specifically, the radial motion of a region on the anterior and of one on the posterior wall–lumen interface was estimated and the difference between the two provided the radial separation of opposite arterial walls throughout the sequence. Because no ECG was recorded, the assumption was subsequently made that the peak of the carotid pressure pulse (loosely referred to as systole) coincided with the maximal radial wall separation. Similarly diastolic images corresponded to the minimal radial separation of the anterior and posterior walls.

The boundary of the atheromatous plaque was outlined on the images by an expert clinician. Fig. 2 shows examples of plaque regions-of-interest (ROIs) manually segmented from images of a symptomatic and an asymptomatic plaque.

B. Selection of Basis Functions

Careful selection of the basis function is a critical issue in a wavelet-transform-based methodology for texture analysis. Such a selection should be based on the desired function properties, including support in time and frequency domain, orthogonality or biorthogonality, symmetry, and shift invariance. The support of a wavelet quantifies its localization in time and frequency domain. It has been shown that, in general, orthogonal filters should be used because they conserve energy and maintain the same amount of energy noise at each level [18]. The symmetry of the filter or, as often referred to in signal analysis, its linear phase is also important for avoiding dephasing. A nonsymmetric filter will result in shift variance of the outputs and this should be avoided in texture analysis.

In this study, a number of basis functions from different wavelet families were used, including Haar (haar), Daubechies (db), symlets (sym), coiflets (coif), and biorthogonal (bior). They have compact support but differ in other properties. The Haar wavelet is orthogonal, symmetric, allows for invariant translations, but has poor frequency localization. Daubechies wavelets are orthogonal but not symmetric. Symlets and coiflets are orthogonal and near symmetric. Biorthogonal wavelets combine many of the properties of the other families. They are symmetric with optimum time/frequency localization; however, they are not shift invariant.

The wavelet functions selected are of small support width because the size of the investigated images was small. Using higher support widths would lead to unreasonably increased values beyond the third level of analysis.

C. Texture Feature Extraction and Selection

The level of decomposition for each scheme was determined according to the best level of decomposition for WP. The best level algorithm based on an entropy criterion among the complete subimages was applied, which indicated three levels of decomposition.

The detail subimages contain the textural information in horizontal, vertical, and diagonal orientations. The approximation subimages were not used for texture analysis because they are the rough estimate of the original image and capture the intensity variations induced by lighting. The total number of subimages for three levels of decomposition, including only the detail images, was 9 in the case of DWT and SWT, 63 in the case of WP, and 12 in the case of GT. For the GT, the lowest and the highest center frequencies were set to 0.05 and 0.4, respectively. The size of the Gabor filter used for texture feature extraction was 13 $\times$ 13. Gabor texture information was obtained at 0°, 90°, 45°, and 135°.

1) *Multiresolution feature extraction:* The texture features that were estimated from each detail subimage were the mean and standard deviation of the absolute value of detail subimages, both commonly used as texture descriptors [13]

$$\mu_j = \frac{1}{N \cdot M} \sum_{x=1}^{N} \sum_{y=1}^{M} |D_j(x,y)| \tag{4}$$

$$\sigma_j = \frac{1}{N \cdot M} \sum_{x=1}^{N} \sum_{y=1}^{M} |D_j(x,y) - \mu_j|^2 \tag{5}$$

where $D_j(x,y)$ are the detail subimages of dimension $N \times M$ in every orientation at level $j = 1$, 2, and 3.

2) *Statistical and fractal feature extraction:* The performance of multiresolution features was compared to that of more "traditional" texture features used in previous similar studies. Specifically, a vector was constructed, consisting of

15 features, which were found dominant in discriminating symptomatic and asymptomatic plaques in a previous study [3]. The features included the GSM, the mean and range values of angular second moment and entropy, the inverse difference moment, the sum average and entropy, the difference variance, the information measure of correlation, the coarseness, the periodicity, the roughness, and the Hurst coefficient (H^k) for $k = 1, 2$.

3) *Feature selection:* Feature selection techniques provide an optimal subset of the original feature representation, which preserves the properties of the data tested and lead to an improved classification performance. In this study, the extracted feature vectors were first sorted in descending order according to the features' divergence value

$$\mathrm{DV}(f_i) = (\sigma_{a,f_i} - \sigma_{s,f_i})^2(1 + \sigma_{a,f_i} + \sigma_{s,f_i})/2\sigma_{a,f_i}\sigma_{s,f_i} \tag{6}$$

where σ_{a,f_i} and σ_{s,f_i} are the standard deviations of the feature vector f_i for asymptomatic and symptomatic plaques, respectively. The DV was used to separate the features because no assumption of the distribution's condition is needed. Then, the nonlinear correlation coefficient (NCC) of two feature vectors of length $N = 20$ (the size of the dataset), based on the normalized mutual information, was used to eliminate not only the linear but also the general dependencies among them [19]

$$\mathrm{NCC}\,(f_a, f_s) = 2 + \sum_{i=1}^{b}\sum_{j=1}^{b} \frac{n_{ij}}{N} \log_b \frac{n_{ij}}{N} \tag{7}$$

where n_{ij} is the number of samples distributed in the *ij* class of the *b* classes of the variables. Its value lies in the closed interval [0, 1], where 0 indicates the minimum and 1 indicates the maximum general correlation of the two vector features. Features were only retained if they produced a NCC value lower than a set threshold. In this study, the threshold used was set to 0.6 after having experimented with a number of different values. NCC values equal to zero were also discarded because they could be attributed to noise.

D. Classification

To address the drawback of the small-sized sample in this study, the resampling method of leave-one-out was used. Leave-one-out is popular among other resampling techniques and has been shown to provide unbiased performance evaluation results [20].

1) *Probabilistic neural networks:* PNN, a type of artificial neural networks, consist of three layers: one input layer with number of neurons equal to the number of used features, a hidden layer also known as summation layer, and an output layer. In order to classify a subject, the corresponding feature vector f_i is applied to the input layer, which computes distances of the feature vector f_i from the feature vectors of all cases in the training set. In the summation layer, a probabilistic density function $p(f_i/C)$, where C is the class for symptomatic and asymptomatic cases, is estimated taking into account the classes to which a number of training examples of the training set belong to. The output neuron classifies the input feature vector into the class with the highest probabilistic density function. Several values for the spread function S, defining the number of training examples taken into account for the classification of a new feature vector, were used $S = \{0.005, 0.0075, 0.01, 0.05, 0.1, 0.5\}$ and the best values were selected on a trial-and-error basis. Additional information about the PNN approach may be found in [15].
2) *Support vector machines:* SVM are learning machines based on intuitive geometric principles, aiming to the definition of an optimal hyperplane, which separates the training data so that a minimum expected risk is achieved. Using the SVM approach, a decision function *df(s)* that can correctly classify an input pattern s is constructed after the training phase of the classifier. The training method is based on a nonlinear mapping of the dataset, using kernels that have to satisfy Mercer's theorem. In this study, the performance of the Gaussian radial basis function (RBF) kernel has been investigated. This kernel seemed to provide better results than other considered kernels (such as the sigmoid and the polynomial kernel). Additional information about the SVM approach may be found in [21].
The LIBSVM library [22] was used along with the leave-one-out method for performance evaluation. To apply the SVM training algorithm, two parameters have to be adjusted, the regularization parameter P and the parameter g for the Gaussian kernel. Parameterization was applied for the following values of parameters: $P \in \{2^{-3}, 2^{-2}, \ldots, 2^{15}\}$, $g \in \{2^{-12}, 2^{-11}, \ldots, 2^{4}\}$ using tenfold cross validation.
3) *Classification performance:* In addition to classification accuracy, the sensitivity (SN) and the specificity (SP) were also estimated. SN (SP) is the ratio of the number of cases correctly classified as symptomatic (asymptomatic) over the total number of actually symptomatic (asymptomatic) cases.

IV. Results

Table I shows the classification results for the two classifiers and all feature sets. The highest accuracy scores in the SVM case for each decomposition scheme (indicated by bold type in the table) were as follows. For DWT, the bior3.3 in systole and haar in diastole yielded the highest value (80%). For SWT, the bior3.1 in systole and bior3.1, bior3.3 and db6 in diastole all scored 75%. For WP, coif1, and coif2 in systole and coif1 in diastole produced 75% and 90% performance, respectively. GT yielded an accuracy of 85% for systole and 65% for diastole. The statistical features set (STATS) achieved an accuracy of 70% for systole and 65% for diastole.

The highest accuracy scores in the PNN case for each decomposition scheme (indicated by bold type in the table) were as follows. For DWT, the db4 in systole and sym3 in diastole produced 65% and 70% performance, respectively. For SWT,

TABLE I
CLASSIFICATION RESULTS FOR DIFFERENT WAVELET FAMILIES AND MULTIRESOLUTION SCHEMES

Multiresolution Scheme	Features		Classification performance (%)					
			Probabilistic neural networks			Support vector machines		
	Extracted	Selected	ACC	SN	SP	ACC	SN	SP
DWT (bior3.1, L=3)	18	7 (9)	60 (65)	63.6 (72.7)	55.6 (55.6)	75 (75)	90.9 (90.9)	55.6 (55.6)
DWT (bior3.3, L=3)	18	7 (10)	55 (60)	54.5 (72.7)	55.6 (44.4)	**80** (60)	81.8 (81.8)	77.8 (33.3)
DWT (bior4.4, L=3)	18	6 (10)	60 (50)	72.7 (54.5)	44.4 (44.4)	70 (65)	81.8 (81.8)	55.6 (44.4)
DWT (haar, L=3)	18	5 (5)	40 (60)	45.5 (63.6)	33.3 (55.6)	65 (**80**)	63.6 (81.8)	66.7 (77.8)
DWT (db4, L=3)	18	6 (12)	**65** (65)	81.8 (72.7)	44.4 (55.6)	75 (55)	81.8 (72.7)	66.7 (33.3)
DWT (db6, L=3)	18	9 (8)	55 (55)	63.6 (63.6)	44.4 (44.4)	70 (60)	72.7 (54.5)	66.7 (66.7)
DWT (sym3, L=3)	18	9 (9)	60 (**70**)	72.7 (63.6)	44.4 (77.8)	75 (70)	72.7 (63.6)	77.8 (77.8)
DWT (sym5, L=3)	18	9 (11)	60 (55)	63.6 (63.6)	55.6 (44.4)	75 (70)	72.7 (72.7)	77.8 (66.7)
DWT (coif1, L=3)	18	8 (6)	50 (60)	63.6 (63.6)	33.3 (55.6)	75 (65)	81.8 (63.6)	66.7 (66.7)
DWT (coif2, L=3)	18	8 (13)	45 (55)	45.5 (63.6)	44.4 (44.4)	60 (55)	72.7 (63.6)	44.4 (44.4)
SWT (bior3.1, L=3)	18	3 (4)	40 (70)	36.4 (81.8)	44.4 (55.6)	**75** (**75**)	81.8 (81.8)	66.7 (66.7)
SWT (bior3.3, L=3)	18	5 (4)	45 (75)	45.5 (72.7)	44.4 (77.8)	65 (**75**)	72.7 (72.7)	55.6 (77.8)
SWT (bior4.4, L=3)	18	5 (6)	45 (70)	45.5 (81.8)	44.4 (55.6)	70 (70)	72.7 (63.6)	66.7 (77.8)
SWT (haar, L=3)	18	3 (5)	35 (55)	27.3 (54.5)	44.4 (55.6)	65 (55)	54.5 (72.7)	77.8 (33.3)
SWT (db4, L=3)	18	6 (4)	50 (70)	45.5 (81.8)	55.6 (55.6)	70 (60)	72.7 (63.6)	66.7 (55.6)
SWT (db6, L=3)	18	6 (5)	45 (75)	36.4 (81.8)	55.6 (66.7)	55 (**75**)	45.5 (72.7)	66.7 (77.8)
SWT (sym3, L=3)	18	5 (4)	45 (**80**)	45.5 (90.9)	44.4 (66.7)	70 (65)	72.7 (72.7)	66.7 (55.6)
SWT (sym5, L=3)	18	5 (5)	**55** (70)	54.5 (81.8)	55.6 (55.6)	70 (60)	63.6 (63.6)	77.8 (55.6)
SWT (coif1, L=3)	18	3 (6)	35 (**80**)	36.4 (90.9)	33.3 (66.7)	70 (70)	63.6 (63.6)	77.8 (77.8)
SWT (coif2, L=3)	18	5 (4)	50 (65)	54.5 (72.7)	44.4 (55.6)	70 (65)	72.7 (63.6)	66.7 (66.7)
WP (bior3.1, L=3)	126	7 (14)	50 (65)	45.5 (54.5)	55.6 (77.8)	70 (55)	63.6 (72.7)	77.8 (33.3)
WP (bior3.3, L=3)	126	13 (20)	55 (65)	54.5 (72.7)	55.6 (55.6)	70 (65)	72.7 (63.6)	66.7 (66.7)
WP (bior4.4, L=3)	126	13 (20)	50 (65)	45.5 (72.7)	55.6 (55.6)	65 (65)	72.7 (63.6)	55.6 (66.7)
WP (haar, L=3)	126	4 (10)	**70** (60)	72.7 (54.5)	66.7 (66.7)	70 (85)	72.7 (90.9)	66.7 (77.8)
WP (db4, L=3)	126	14 (23)	60 (60)	45.5 (63.6)	77.8 (55.6)	65 (55)	81.8 (54.5)	44.4 (55.6)
WP (db6, L=3)	126	14 (18)	55 (55)	54.5 (63.6)	55.6 (44.4)	45 (70)	45.5 (72.7)	44.4 (66.7)
WP (sym3, L=3)	126	15 (17)	60 (60)	54.5 (72.7)	66.7 (44.4)	70 (70)	63.6 (63.6)	77.8 (77.8)
WP (sym5, L=3)	126	12 (17)	45 (55)	45.5 (45.5)	44.4 (66.7)	70 (75)	63.6 (81.8)	77.8 (66.7)
WP (coif1, L=3)	126	11 (10)	65 (**70**)	72.7 (81.8)	55.6 (55.6)	**75** (**90**)	81.8 (90.9)	66.7 (88.9)
WP (coif2, L=3)	126	10 (18)	60 (60)	63.6 (63.6)	55.6 (55.6)	**75** (70)	63.6 (100)	88.9 (33.3)
GT	24	13 (9)	**75** (55)	72.7 (54.5)	77.8 (55.6)	**85** (65)	81.8 (54.6)	88.9 (77.8)
STATS	15	7 (8)	**55** (50)	63.6 (72.7)	44.4 (22.2)	**70** (65)	72.7 (72.7)	55.6 (66.7)

ACC: Accuracy, SN: Sensitivity, SP: Specificity, and L: number of decomposition levels. bior: biorthogonal, db: daubechies, sym: symlet, coif: coiflet, and STATS: statistical and fractal feature set. Values in parentheses correspond to diastole; the others to systole. Bold characters correspond to the highest accuracy scores in each decomposition scheme.

the sym5 in systole (55%) and sym3 and coif1 in diastole scored 80%. For WP, haar in systole and coif1 in diastole all produced 70%. GT yielded an accuracy of 75% for systole and 55% for diastole. STATS achieved an accuracy of 55% for systole and 50% for diastole.

Overall, for both classifiers, WP combined with coif1 produced the highest overall accuracy for systole and diastole (82.5% and 67.5%, respectively, for SVM and PNN), followed by WP combined with haar (77.5% and 65%, respectively, for SVM and PNN).

For SVM, if the average accuracy over all investigated basis functions is considered, the GT was best (75%), followed by DWT together with WP (68.8%), and SWT together with STATS by 67.5%. For PNN, the GT was also best (65%) followed by WP (59.3%), SWT (57.8%), DWT (57.3%), and STATS (52.3%).

With respect to the other investigated classification performance parameters, i.e., SN and SP, the aforementioned decomposition scheme-wavelet combinations generally produced highest values in these parameters as well.

Table II shows the average ($\pm$std) values of the selected features for WP with coif1 and SVM, for systole and diastole, the combination that produced the highest overall accuracy. As we can see, most of these correspond to horizontal subimages. Also, the DV values in systole were significantly higher than in diastole (p-value < 0.05).

TABLE II
EXAMPLES OF MEAN ($\pm$STD) AND DIVERGENCE (DV) VALUES OF THE SELECTED FEATURES USING WP AND COIF1

Subimage's Feature	Asymptomatic	Symptomatic	DV
Systole			
Mean (μ)			
$Dh_3A_2Dh_1$	1.989±0.502	3.732±1.911	12.73
$Dh_3Dh_2Dh_1$	0.002±0.001	0.003±0.002	6.81
Dh_2Dh_1	0.005±0.003	0.011±0.008	6.75
$Dh_3Dh_2A_1$	0.025±0.013	0.047±0.035	5.79
Dh_1	15.425±4.775	25.081±11.311	5.37
Std (σ)			
$Dh_3A_2Dh_1$	0.003±0.002	0.009±0.006	13.76
$Dh_3Dv_2A_1$	0.003±0.001	0.005±0.003	4.89
$Dh_3Dh_2Dh_1$	0.001±0.000	0.001±0.000	4.83
$Dh_3Dh_2A_1$	0.003±0.002	0.005±0.003	4.44
$Dh_3A_2A_1$	0.001±0.001	0.002±0.001	4.43
Dh_2A_1	2.426±0.755	3.238±0.910	4.32
Diastole			
Mean (μ)			
$Dh_3Dh_2Dh_1$	2.493±0.701	4.124±1.320	7.59
$Dh_3A_2Dh_1$	0.025±0.014	0.044±0.028	5.80
Dh_2Dh_1	0.678±0.266	0.944±0.195	4.87
$Dh_3A_2A_1$	0.002±0.001	0.003±0.002	4.12
$Dh_3Dh_2A_1$	0.005±0.003	0.008±0.004	3.35
Dh_1	0.001±0.001	0.002±0.001	3.25
Dh_2A_1	0.547±0.297	0.637±0.153	3.01
$Dh_3A_2Dh_1$	0.438±0.226	0.519±0.139	2.91
Std (σ)			
$Dh_3A_2A_1$	0.001±0.001	0.002±0.001	2.93
$Dd_3Dd_2Dh_1$	0.001±0.001	0.001±0.001	2.89

V. DISCUSSION

In this study, an in-depth investigation was attempted of the possibility of wavelet transforms to characterize the texture of

carotid atheromatous plaque tissue from B-mode ultrasound images. To this end, 1) four decomposition schemes, namely, DWT, SWT, WP, and GT and 2) a number of basis functions from different wavelet families were investigated. The numerical results produced using combinations of the aforementioned point to some interesting observations. Given that this is one of the first attempts to characterize carotid artery tissue using a scale/frequency approach, the findings of the study may be useful in wavelet-based texture analysis of ultrasound images of arterial tissue.

A recently presented multiresolution approach for the characterization of carotid plaque included the AM–FM representation of the plaque ultrasound image [23]. In this case, the nonstationary image content was modeled in terms of a series expansion of AM–FM component images.

In this study, the performance of SVM was superior to that of PNN for the great majority of the investigated feature sets. A similar finding was also reported in [15]. SVM is an efficient classification method, which compared to other classifiers, is less affected by the so-called "curse of dimensionality" [24]. Thus, the large number of features provided by the multiresolution methods investigated here, allow SVM to yield relatively high classification rates.

A crucial issue that should be clarified in the context of this study is which wavelet transform would be more appropriate for the application under interrogation. According to our experimental results, although drawn from a limited dataset, WP combined with the coif1 outperformed the other investigated combinations in terms of the overall accuracy. By definition, WP provide a richer spatial/frequency representation, including high-, medium-, and low-frequency information, which is desirable for ultrasound images of the carotid artery. On the other hand, the other decomposition schemes are usually constrained to low-frequency information, which might not be adequate for classification [25]. Based on the earlier analysis, it is suggested that WP would be more appropriate for wavelet-based texture analysis of ultrasound images of the carotid atheromatous plaque.

Appropriate choice of the basis function is another key issue for efficient wavelet-based texture analysis. In the WP case, coif1 followed by haar yielded the highest overall performance values, 82.5% and 77.5%, respectively (see Table I). In addition to this, according to recommendations in a previous study [18], the desired properties of basis functions for texture analysis should include orthogonality (all interrogated wavelets were orthogonal), symmetry (haar and bior), and shift invariance (only haar in the case of DWT and WP, whereas SWT allows for invariant properties because downsampling is avoided). Based on the earlier analysis, it is suggested that the near symmetric orthogonal coif1 could be used for WP analysis of ultrasound images of carotid atherosclerotic plaque.

Previous studies on texture-based classification of carotid atherosclerotic plaque from B-mode ultrasound yielded various performances. Christodoulou *et al*. [3] reported a classification performance of 73.1% using a variety of texture features and self-organizing maps. Mougiakakou *et al*. [26] reached 99.1% classification using statistical and laws' texture features and genetic algorithms. The more recent multiscale studies, including AM–FM representation [23] and multilevel morphological analysis [15], reached 71.5% and 73.7% accuracy, respectively. Because the datasets, image analysis methods and classifiers used in these studies are different, a direct comparison cannot be attempted. However, it could be argued that WP analysis in combination with SVM can be considered efficient for texture classification of carotid plaque from B-mode ultrasound.

According to [27], compared to DWT, the SWT multiresolution scheme is less dependent on the wavelet filter and a reasonable choice could only be resorted to application considerations. In our study, compared to the other decomposition schemes, the SWT produced less variability in terms of the accuracy values both for systole and diastole, especially when SVM was used. This, in combination with the fair performance of SWT (67.5% accuracy on average in the SVM case), might be an acceptable choice if one is unsure about which decomposition scheme and/or basis function to select.

The somewhat different findings produced for different phases of the cardiac cycle, namely, systole and diastole, might be due to slight differences in the allocation of material within the plaque, which may be reflected in the analysis of texture. Related to this, is the fact that the DV values were significantly higher in the systolic images (see Table II), which may suggest greater discriminative ability in this phase of the cardiac cycle. At this point, one should note that for systole, the highest classification accuracy was achieved by the GT using SVM (85%, Table I), suggesting that for systolic images, the GT might be a reasonable choice. Accordingly, it is advisable that texture analysis should be made for the same cardiac cycle phase for all images of the investigated population.

The selected features for WP using coif1 corresponded mostly to the horizontal direction (see Table II). It is possible that the strains experienced by the arterial tissue during the cardiac cycle, due mostly to blood pressure and blood flow, affect the distribution of material within the plaque, which in turn affects the image appearance and the estimated texture. It would, therefore, be interesting to attempt to investigate the strain field of plaques with different texture values using an established motion analysis methodology [17].

The performance of the more "traditional," i.e., statistical and fractal, features was inferior to that of the multiresolution features, yielding an accuracy of 67.5% using SVM. This value is similar to that reported in a previous study [3], using the same feature set along with self-organizing map (68%) and the *k*-nearest neighbor (66.9%) as classifiers. When used alone, the performance of GSM, a common measure of ultrasound image echogenicity, yielded 62.5% overall accuracy using SVM. Given the higher classification accuracy (82%) of WP with coif1, this technique may be considered a better alternative for characterizing atheromatous plaque tissue. The superiority of multiresolution techniques over more "traditional" ones might be due to their ability to capture both the frequency and spatial content of the image by filtering in specific directions and providing features that contain directional information; such information is not captured by "traditional" features.

VI. Conclusion

This study demonstrated that wavelet-based texture analysis may be promising for characterizing atheromatous tissue. As an initial approach, we suggest using WP decomposition with coiflet1 and SVM for such applications. An interesting collateral finding was that biomechanical factors, namely, plaque strains during the cardiac cycle, may be important in the analysis of texture. Additional studies, systematically applying the proposed methodology to larger populations, are expected to corroborate our findings.

References

[1] M. L. Grønholdt, B. G. Nordestgaard, T. V. Schroeder, S. Vorstrup, and H. Sillesen, "Ultrasonic echolucent carotid plaques predict future strokes," *Circulation*, vol. 104, no. 1, pp. 68–73, Jul. 2001.

[2] J. E. Wilhjelm, M. L. M. Grønholdt, B. Wiebe, S. K. Jespersen, L. K. Hansen, and H. Sillesen, "Quantitative analysis of ultrasound B-mode images of carotid atherosclerotic plaque: Correlation with visual classification and histological examination," *IEEE Trans. Med. Imag.*, vol. 17, no. 6, pp. 910–922, Dec. 1998.

[3] C. I. Christodoulou, C.S. Pattichis, M. Pantziaris, and A. N. Nicolaides, "Texture-based classification of atherosclerotic carotid plaques," *IEEE Trans. Med. Imag.*, vol. 22, no. 7, pp. 902–912, Jul. 2003.

[4] I. Mayor, S. Momjian, P. Lalive, and R. Sztajzel, "Carotid plaque: Comparison between visual and grey-scale median analysis," *Ultrasound Med. Biol.*, vol. 29, no. 7, pp. 961–966, Jul. 2003.

[5] T. J. Tegos, M. M. Sabetai, A. N. Nicolaides, T. S. Elatrozy, S. Dhanjil, and J. M. Stevens, "Patterns of brain computed tomography infarction and carotid plaque echogenicity," *J. Vasc. Surg.*, vol. 33, no. 2, pp. 334–339, Feb. 2001.

[6] P. Asvestas, S. Golemati, G. K. Matsopoulos, K. S. Nikita, and A. N. Nicolaides, "Fractal dimension estimation of carotid atherosclerotic plaques from B-mode ultrasound: A pilot study," *Ultrasound Med. Biol.*, vol. 28, no. 9, pp. 1129–1136, Sep. 2002.

[7] E. Kyriacou, C. Pattichis, M. Pattichis, C. Loizou, C. Christodoulou, S. Kakkos, and A. Nicolaides, "A review of noninvasive ultrasound image processing methods in the analysis of carotid plaque morphology for the assessment of stroke," *IEEE Trans. Inf. Technol. Biomed.*, vol. 14, no. 4, pp. 1027–1038, Jul. 2010.

[8] P. N. T. Wells and M. Halliwell, "Speckle in ultrasonic imaging," *Ultrasonics*, vol. 19, no. 5, pp. 225–229, Sep. 1981.

[9] M. Mojsilovic, M. V. Popovic, A. N. Neskovic, and A. D. Popovic, "Wavelet image extension for analysis and classification of infracted myocardial tissue," *IEEE Trans. Biomed. Eng.*, vol. 44, no. 9, pp. 856–866, Sep. 1997.

[10] D.-R. Chen, R.-F. Chang, W.-J. Kuo, M.-C. Chen, and Y.-L. Huang, "Diagnosis of breast tumors with sonographic texture analysis using wavelet transform and neural networks," *Ultrasound Med. Biol.*, vol. 28, no. 10, pp. 1301–1310, Oct. 2002.

[11] S. Li and J. Shawe-Taylor, "Comparison and fusion of multiresolution features for texture classification," *Pattern Recogn. Lett.*, vol. 26, pp. 633–638, Apr. 2005.

[12] K. Huang and S. Aviyente, "Information-theoretic wavelet packet subband selection for texture classification," *Signal Process.*, vol. 86, no. 7, pp. 1410–1420, Jul. 2006.

[13] H. Yoshida, D. D. Casalino, B. Keserci, A. Coskun, O. Ozturk, and A. Savranlar, "Wavelet-packet-based texture analysis for differentiation between benign and malignant liver tumours in ultrasound images," *Phys. Med. Biol.*, vol. 48, pp. 3735–3753, Nov. 2003.

[14] J. Stoitsis, S. Golemati, N. Tsiaparas, and K. S. Nikita, "Texture characterization of carotid atherosclerotic plaque from B-mode ultrasound using Gabor filters," in *Proc IEEE Conf. Eng. Med. Biol. Soc.*, 2009, vol. 2009, pp. 455–458.

[15] E. Kyriacou, M. S. Pattichis, C. S. Pattichis, A. Mavrommatis, C. I. Christodoulou, S. Kakkos, and A. Nicolaides, "Classification of atherosclerotic carotid plaques using morphological analysis on ultrasound images," *Appl. Intell.*, vol. 30, no. 1, pp. 3–23, Feb. 2009.

[16] I. Daubechies, *Ten Lectures on Wavelets*. Philadelphia, PA: Society for Industrial and Applied Mathematics, 1992.

[17] S. Golemati, A. Sassano, M. J. Lever, A. A. Bharath, S. Dhanjil, and A. N. Nicolaides, "Motion analysis of carotid atherosclerotic plaque from B-mode ultrasound," *Ultrasound Med. Biol.*, vol. 29, no. 3, pp. 387–399, Mar. 2003.

[18] A. Mojsilovic, M. V. Popovic, and D. Rackov, "On the selection of an optimal wavelet basis for texture characterization," *IEEE Trans. Imag. Process.*, vol. 9, no. 12, pp. 2043–2050, Dec. 2000.

[19] Q. Wang, Y. Shen, and J. Q. Zhang, "A nonlinear correlation measure for multivariate data set," *Physica D*, vol. 200, no. 3–4, pp. 287–295, Jan. 2005.

[20] Q. Li and K. Doi, "Comparison of typical evaluation methods for computer-aided diagnostic schemes: Monte Carlo simulation study," *Med. Phys.*, vol. 34, no. 3, pp. 871–876, Mar. 2007.

[21] C. J. C. Burges, "A tutorial on support vector machines for pattern recognition," *Data Min. Knowl. Disc.*, vol. 2, no. 2, pp. 1–43, Jun. 1998.

[22] C.-C. Chang C.-J. Lin (2001). *LIBSVM: A library for support vector machines.* Software available at http://www.csie.ntu.edu.tw/∼cjlin/libsvm.

[23] C. I. Christodoulou, C. S. Pattichis, V. Murray, M. S. Pattichis, and A. Nicolaides, "AM-FM representations for the characterization of carotid plaque ultrasound images," *IFMBE Proc.*, vol. 22, pp. 546–549, 2009.

[24] L. Shutao, J. T. Kwok, H. Zhu, and Y. Wang, "Texture classification using support vector machines," *Pattern Recogn.*, vol. 36, no. 12, pp. 2883–2893, Dec. 2003.

[25] T. Chang and C.-C. J. Kuo, "Texture analysis and classification with tree-structured wavelet transform," *IEEE Trans. Imag. Process.*, vol. 2, no. 4, pp. 429–441, Oct. 1993.

[26] S. G. Mougiakakou, S. Golemati, I. Gousias, A. N. Nicolaides, and K. S. Nikita, "Computer-aided diagnosis of carotid atherosclerosis based on ultrasound image statistics, Laws' texture and neural networks," *Ultrasound Med. Biol.*, vol. 33, no. 1, pp. 26–36, Jan. 2007.

[27] D. B. Percival and A. T. Walden, *Wavelet Methods for Time Series Analysis*. Cambridge: Cambridge Univ. Press, 2000.

Nikolaos N. Tsiaparas received the degree of Mathematics from the University of Crete, Crete, Greece, in 2002, the M.Sc. degree in advanced photonics and communications from the University of Warwick, Coventry, U.K., in 2003, and the M.Sc. degree in biomedical engineering from the University of Patras, Patras, Greece, in 2006. He is currently working toward the Ph.D. degree with the Biomedical Simulations and Imaging Laboratory, School of Electrical and Computer Engineering, National Technical University of Athens, Athens, Greece.

His research interests include biomedical image and signal processing focused on wavelet, ridgelet and curvelet transforms. He has authored or coauthored nine papers in international journals and conferences.

Mr. Tsiaparas is a member of Professional Chamber of Greece.

Spyretta Golemati received the Diploma in mechanical engineering from the National Technical University of Athens, Athens, Greece, in 1994, and the M.Sc. and Ph.D. degrees in bioengineering from Imperial College of Science, Technology, and Medicine, University of London, London, U.K., in 1995 and 2000, respectively.

She then was a Postdoctoral Fellow in the Department of Electrical and Computer Engineering, National Technical University of Athens, Athens, Greece. She is currently a Lecturer in Biomedical Engineering in the National Kapodistrian University of Athens, Greece. Her research interests include medical image and signal processing, arterial biomechanics, and respiratory mechanics. She has coauthored 20 papers in international scientific journals, eight book chapters, and 29 papers in international conference proceedings.

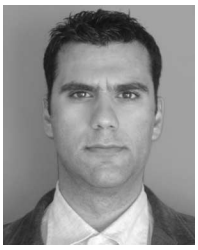

Ioannis Andreadis was born in Athens, Greece in 1984. He received the degree in electrical and computer engineering in 2006 from the National Technical University of Athens, Athens, Greece, where he is currently working toward the Ph.D. degree.

Since 2007, he has been with the Biomedical Simulation and Imaging Laboratory, Department of Electrical and Computer Engineering, National Technical University of Athens. He has authored or co-authored of nine international journal and conference papers. His main research interests include image processing and analysis, mainly concentrating on medical images, and artificial intelligence.

John S. Stoitsis received the Diploma in electrical and computer engineering from the Aristotle University of Thessaloniki, Thessaloniki, Greece, in 2002, and the M.Sc. and Ph.D. degrees in biomedical engineering from the University of Patras, Patras, Greece, in 2004 and 2007, respectively.

His research interests include biomedical image and signal processing, medical informatics, and computer aided diagnosis. He has authored or co-authored nine papers in international journals and chapters in books, and more than 20 papers in international conferences. He has participated (as a project manager or research associate) in several EU-funded and National Research initiatives.

Dr. Stoitsis is a member of the Institute of Electrical and Electronics Engineers and the Technical Chamber of Greece.

Ioannis Valavanis received the Diploma in electrical and computer engineering from the National Technical University of Athens (NTUA), Athens, Greece, in 2003, the M.Sc. degree in bioinformatics from the University of Athens, Athens, Greece, in 2006, and the Ph.D. degree from NTUA in 2009.

His Ph.D. research included the development and use of network-based methods for the analysis of protein structural/sequence data and data related to multifactorial diseases. He has also worked in the areas of microarrays analysis, structural bioinformatics, image processing, and decision support systems. His current research interests include bioinformatics, medical and genetic data analysis, artificial intelligence and its applications. He is the coauthor of 24 articles published in international journals and conferences or published as book chapters. He has participated in several EU-funded and National Research initiatives. He is currently with the National Hellenic Research Foundation, Greece, and the School of Electrical and Computer Engineering, NTUA as a Postdoctoral Research Fellow, and is a Visiting Faculty Member at the Technical Educational Institute of Chalkida, Greece.

Dr. Valavanis is a member of the Institute of Electrical and Electronics Engineers and the Technical Chamber of Greece.

Konstantina S. Nikita (SM'00) received the Diploma in electrical engineering and the Ph.D. degree from the National Technical University of Athens (NTUA), Athens, Greece. She then received the M.D. degree from the Medical School, University of Athens, Athens.

Since 1990, she has been working as a Researcher at the Institute of Communication and Computer Systems, NTUA. In 1996, she joined the Department of Electrical and Computer Engineering, NTUA, as an Assistant Professor, and since 2005, she serves as a Professor, at the same department. Her current research interests include biomedical signal and image processing and analysis, biomedical informatics, simulation of physiological systems, medical imaging, biological effects, and medical applications of radiofrequency electromagnetic fields. She has authored or coauthored 135 papers in refereed international journals and chapters in books, and more than 250 papers in international conference proceedings. She is the author or coauthor of two books (*Simulation of Physiological Systems and Medical Imaging Systems)* in Greek and co-editor of one book (*Computational Electromagnetics: State of the Art and Future Trends*, Springer) in English. She holds two patents. She has been the Technical Manager of several European and National Research and Development projects in the field of biomedical engineering. She has been chair/member of the program/organizing committee of more than 50 international conferences on the same fields.

Dr. Nikita was the Recipient of the 2003 Bodossakis Foundation Academic Prize for exceptional achievements in "Theory and Applications of Information Technology in Medicine". She has been a member of the Board of Directors of the Hellenic National Academic Recognition and Information Center and a member of the National Council of Research and Technology. She is a member of the Editorial Board of the IEEE TRANSACTIONS ON BIOMEDICAL ENGINEERING and Guest Editor of several international journal issues on biomedical engineering subjects. She is a member of the Technical Chamber of Greece and a member of the Athens Medical Association. She is also the founding Chair and Ambassador of the IEEE-Engineering in Medicine and Biology Society, Greece chapter, Vice Chair of the IEEE Greece Section and the Vice Chair of the School of Electrical and Computer Engineering of the NTUA.